Supporting Information

Vanadium-driven oxygen vacancy modulation in MoO_3 nanosheet cathodes for aqueous zinc-ion batteries

Guan-Min Chen,[a] Ngoc Thanh Thuy Tran,[e] Tuan-Yue Lin,[a] Yi-Chieh Huang,[a] Thanh Tuan Nguyen,[e] Shih-kang Lin[a, d, e, f] and Yu-Ze Chen[*a, b, c]

[a] Department of Materials Science and Engineering, National Cheng Kung University, Tainan City 70101, Taiwan

[b] Program on Key Materials, Academy of Innovative Semiconductor and Sustainable Manufacturing, National Cheng Kung University, Tainan City 70101, Taiwan

[c] Program on Semiconductor Packaging and Testing, Academy of Innovative Semiconductor and Sustainable Manufacturing, National Cheng Kung University, Tainan City 70101, Taiwan

[d] Program on Smart and Sustainable Manufacturing, Academy of Innovative Semiconductor and Sustainable Manufacturing, National Cheng Kung University, Tainan 70101, Taiwan.

[e] Center for Resilience and Intelligence on Sustainable Energy Research (RiSER), National Cheng Kung University, Tainan 70101, Taiwan

[f] Core Facility Center, National Cheng Kung University, Tainan 70101, Taiwan.

* Email address: yzchen@gs.ncku.edu.tw

1. Experimental Section

1.1 Synthesis of vanadium-doped MoO_3

The powder of MoO_3 and vanadium-doped MoO_3 (VMO) were synthesized *via* a hydrothermal method. In a typical procedure, 1.52 g (1.23 mmol) of ammonium heptamolybdate tetrahydrate ($(NH_4)_6Mo_7O_{24}\cdot 4H_2O$) and 0.10 g (0.123 mmol) of ammonium metavanadate (NH_4VO_3), serving as the Mo and V precursors, respectively, were dissolved in 50 mL of deionized water under continuous stirring for 10 min. Subsequently, 9 mL of concentrated nitric acid (70 wt%) was added to adjust the pH to approximately −1, which provides a favorable environment for the growth of molybdenum oxides. After an additional 10 min of stirring, the resulting solution was transferred into a Teflon-lined stainless-steel autoclave and maintained at 100–200 °C for 6–40 h. The obtained suspension was centrifuged and washed repeatedly to remove residual impurities. Each washing cycle involved adding 30 mL of deionized water and 20 mL of ethanol, followed by centrifugation at 7500 rpm for 15 min, which was repeated three times. The final product was dried at 60 °C for 24 h to yield MoO_3 (MO) and V-doped MoO_3 (VMO) powders.

1.2 Materials Characterization

Field-emission scanning electron microscopy (FE-SEM, HITACHI SU-5000) was employed to examine the surface morphology. Powder X-ray diffraction (XRD, Bruker D8 DISCOVER with GADDS) was carried out to identify the crystal structure and phase composition. Raman spectra were recorded to characterize the structure of obtained powders by using Raman spectroscopic system (iHR 550, HORIBA). X-ray photoelectron spectroscopy (XPS, PHI VersaProbe 4) was performed to analyze the surface chemical states, while transmission electron microscopy (TEM, JEOL JEM-2100F CS STEM) combined with selected-area electron diffraction (SAED) and energy-dispersive X-ray spectroscopy (EDS) was used to probe the

crystal lattice and elemental distribution. Specific surface area and pore structure were determined by N_2 adsorption–desorption isotherms using a Micromeritics ASAP 2060 analyzer based on the BET and BJH methods. Electron paramagnetic resonance (EPR, EMXnano BENCH-TOP SYSTEM) was further employed to investigate the presence of oxygen vacancies.

1.3 Battery Performance Evaluation

1.3.1 Preparation of Cathode Slurry and Assembly of Coin Cells

The cathode slurry was prepared by mixing the as-synthesized active material, carbon black, and PVDF binder in a weight ratio of 7:2:1, with 1.8 mL N-methyl-2-pyrrolidone (NMP) as the solvent. The slurry was stirred at room temperature for 3–5 days and then coated onto carbon cloth disks (14 mm in diameter), followed by drying in a vacuum oven at 60 °C for 24 h. Zn foil was punched into 14 mm disks and cleaned sequentially in acetone, isopropanol, ethanol, and deionized water for 5 min each under ultrasonication. CR2032-type coin cells were assembled in the order of cathode case, cathode electrode, separator, Zn foil anode, spacer, spring, and anode cap. A total of 0.06 mL of aqueous electrolyte (2 M $ZnSO_4$ + 0.5 M $Al_2(SO_4)_3$) was added dropwise onto the separator to ensure sufficient wetting. The cells were sealed under a pressure of 1500 psi using a crimping machine.

1.3.2 Basic electrochemical measurement

Cyclic voltammetry (CV) measurements were carried out using a three-electrode system with the prepared electrode as the working electrode, a platinum foil as the counter electrode, and Ag/AgCl as the reference electrode. The tests were conducted in 2 M $ZnSO_4$ aqueous electrolyte within a potential window of 0.2–1.2 V (vs. Zn^{2+}/Zn). The potential was swept at scan rates ranging from 0.1 to 2 mV s^{-1} (BioLogic VSP). Electrochemical impedance spectroscopy (EIS) was conducted by applying a small sinusoidal AC perturbation (typically 5–10 mV) over a selected frequency range (BioLogic VSP). The impedance responses were

collected and analyzed in a Nyquist plot. These data were used to extract information on charge-transfer resistance, ion diffusion, and electrode–electrolyte interfacial properties. Galvanostatic charge–discharge (GCD) tests were carried out on a Zn electrode half-cell within the voltage window of 0.3–1.2 V at the current densities of 1 A g^{-1}. The voltage profiles were recorded to calculate the specific capacitance, rate capability, and cycling stability of the electrodes battery testing system (BT-4008Tn, NEWARE).

1.3.3 Diffusivity of Zn^{2+} in Vanadium-doped MoO_3

Galvanostatic intermittent titration technique (GITT) was employed to investigate the Zn^{2+} diffusion behavior of VMO (0.1:1) and pristine MO electrodes during the charge–discharge process. For the measurements, the cells were initially discharged to 0.3 V and subsequently operated at a current density of 0.3 A g^{-1}. A constant current pulse was applied for 1 min, followed by a relaxation period of 2 min to allow the voltage to reach equilibrium. This procedure was repeated until the potential increased to 1.0 V, after which the same condition was applied during the subsequent discharge down to 0.3 V. During each charge–discharge step of the GITT measurement, the potential response can be divided into two regions: the instantaneous potential change (ΔE_t) upon applying the current pulse, and the steady-state potential change (ΔE_s) after the relaxation period. The difference between ΔE_t and ΔE_s reflects the resistance associated with ion transport from the electrolyte into the electrode bulk. According to the GITT model, the Zn^{2+} diffusion coefficient (D) was calculated using the following relation:[1]

$$D^{GITT} = \frac{4}{\pi\tau}\left(\frac{m_B}{\rho S}\right)^2\left(\frac{\Delta E_s}{\Delta E_t}\right)^2$$

where τ is the relaxation time, m_B is the mass of the active material, and ρ are the density of the active materials and S is the electrode–electrolyte contact area.

2. Computational Methods

First-principles calculations were carried out using the Vienna Ab initio Simulation Package (VASP),[2] which employs the projector augmented-wave (PAW) method within the framework of density functional theory (DFT).[3-5] The generalized gradient approximation (GGA) with the Perdew–Burke–Ernzerhof (PBE) exchange-correlation functional was used to investigate the structural and electronic properties of pristine and V-doped MoO_3.[6] To account for strong on-site Coulomb interactions, DFT+U calculations were employed, with Hubbard U values of 4.38 eV for Mo and 3.25 eV for V.[7] The simulation model consisted of a 2 × 1 × 1 supercell containing 8 Mo atoms (or 7 Mo and 1 V atom for the doped system) and 24 O atoms. Based on total energy comparisons, the most energetically favorable V doping configuration was chosen for subsequent electronic structure and diffusion analyses. Brillouin zone integration was performed using a Γ-centered 2 × 1 × 4 k-point mesh for geometry optimizations and a denser 4 × 2 × 8 mesh for density of states (DOS) calculations. All atomic positions and lattice parameters were fully relaxed until the residual forces were below 0.01 eV $Å^{-1}$ and the total energy converged within 10^{-5} eV. A plane-wave energy cutoff of 520 eV was used. Spin polarization was included to examine potential magnetic behavior. To evaluate Zn-ion migration barriers in pristine and V-doped MoO_3, the climbing image nudged elastic band (CI-NEB) method was applied. [8, 9] The minimum energy paths were determined between relaxed initial and final states using three intermediate images for computational efficiency.

Table S1 V contents of MO and V-doped MoO_3 samples determined by ICP–MASS.

	MO	VMO(0.05:1)	VMO(0.1:1)	VMO(0.2:1)	VMO(1:1)
V%	0	0.4%	0.6	1.1	3.4

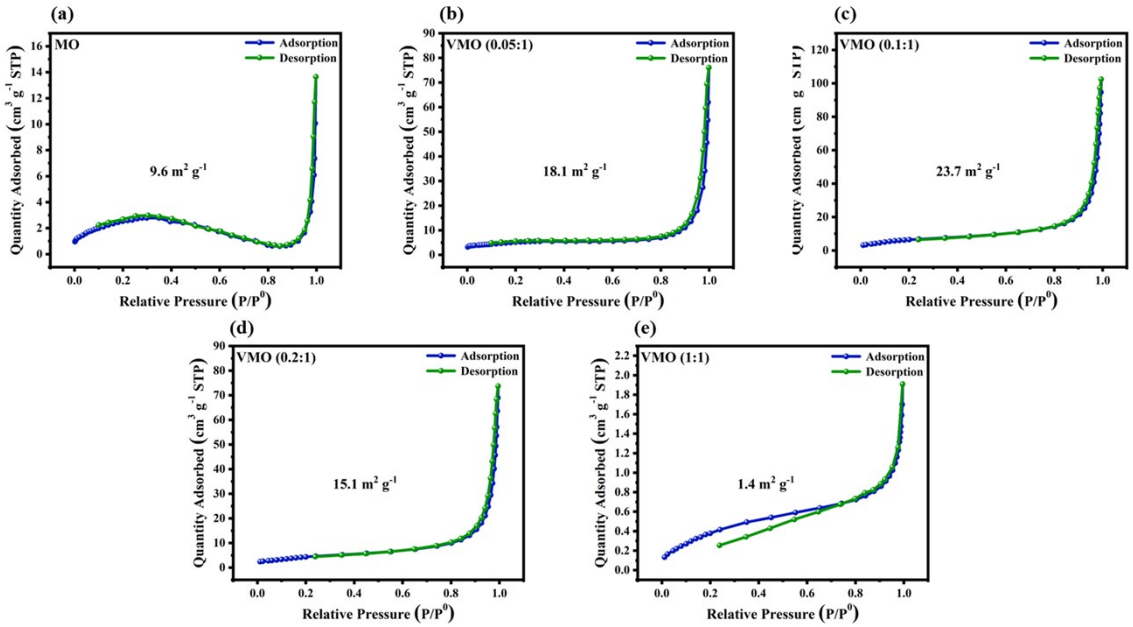

Figure S1 Nitrogen adsorption–desorption isotherms of (a) MO, (b) VMO (0.05:1), (c) VMO (0.1:1), (d) VMO (0.2:1), and (e) VMO (1:1) measured at 77 K.

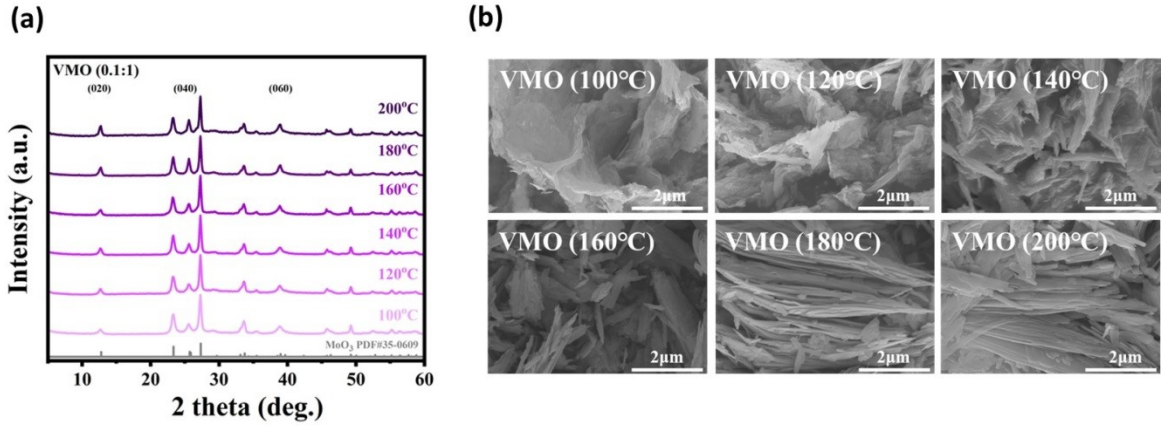

Figure S2 (a) XRD patterns of VMO(0.1:1) at different hydrothermal temperatures, confirming phase stability. (b) SEM images showing morphology evolution from silk-like networks (100-120 °C) to mixed nanorods/nanosheets (140-160 °C) and finally stacked nanosheets (180-200 °C).

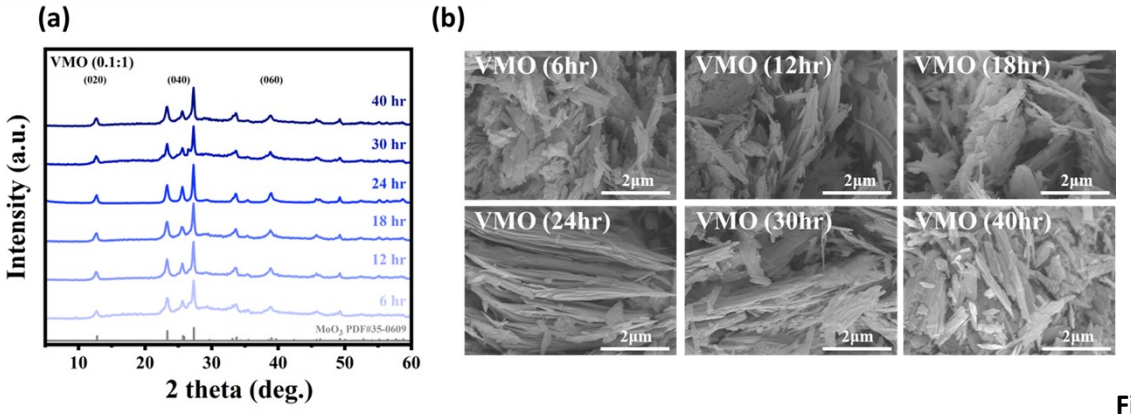

Figure S3 (a) XRD patterns of VMO(0.1:1) at different hydrothermal reaction duration. (b) SEM images showing morphology evolution, showing the time-dependent morphological evolution from irregular nanorod/nanosheet aggregates to well-defined nanosheet-stacked structures (optimal at 24 h), followed by re-aggregation at longer durations.

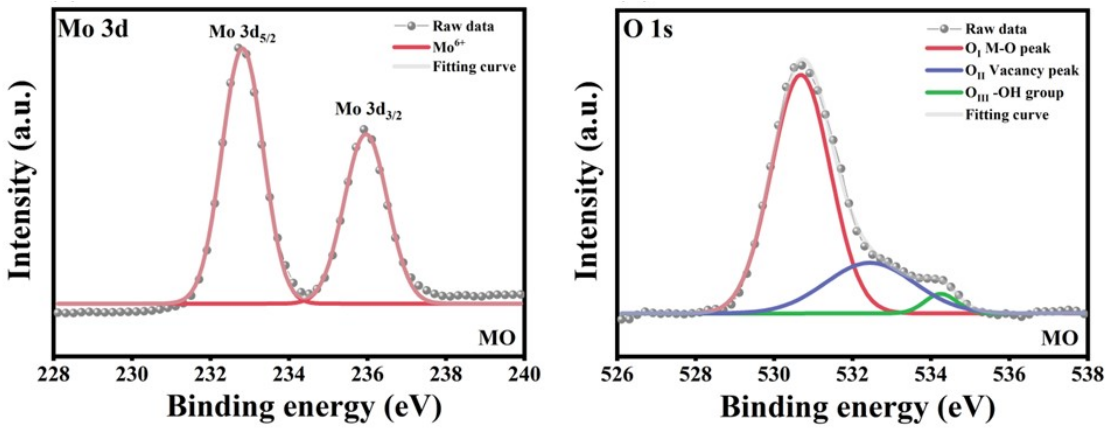

Figure S4 XPS spectra of MO. (a) Mo 3d peaks, and (b) O 1s peaks.

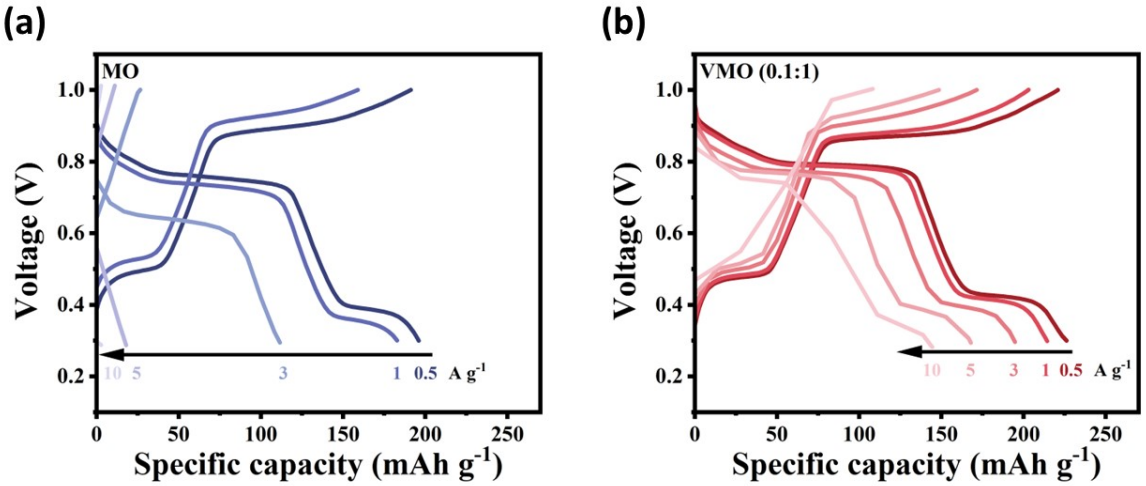

Figure S5 Galvanostatic charge–discharge curves of MO and VMO (0.1:1) at different current densities.

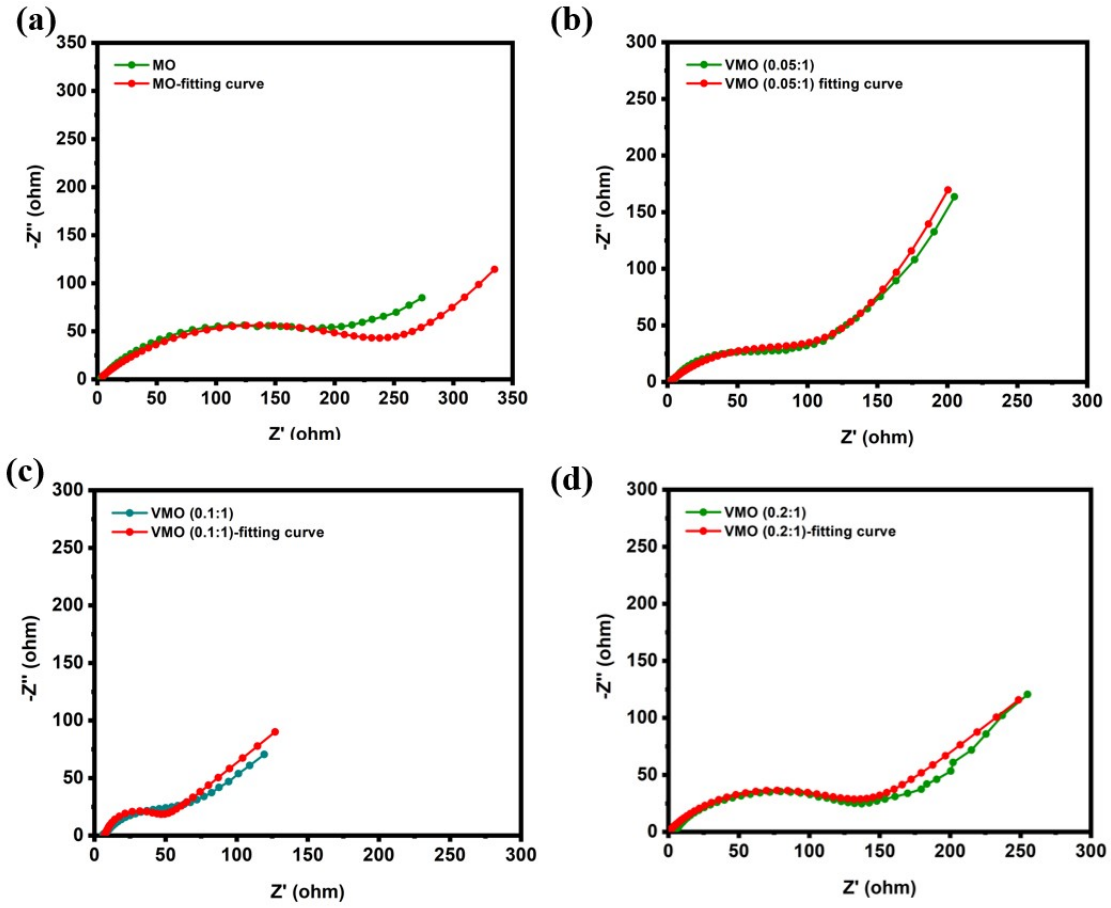

Figure S6 Nyquist plots and corresponding fitting curves of (a) MO, (b) VMO (0.05:1), (c) VMO (0.1:1), and (d) VMO (0.2:1).

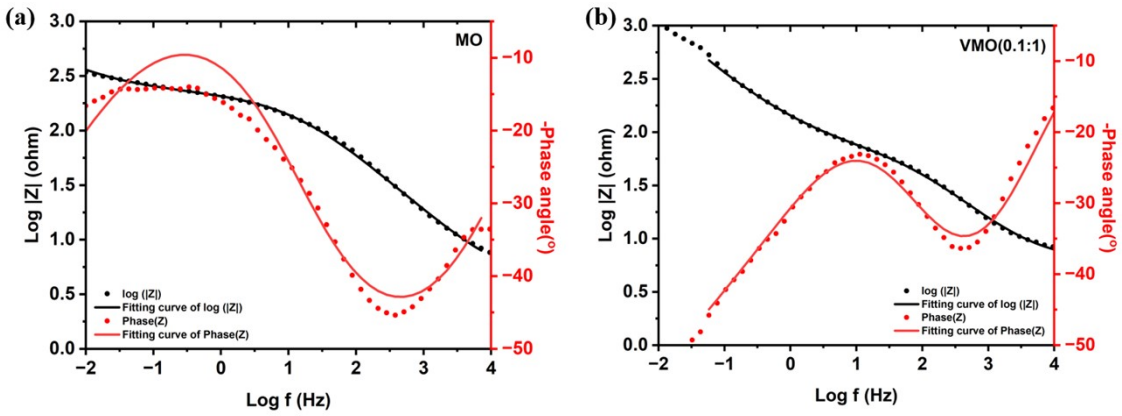

Figure S7 Bode plots of (a)MO and (b)VMO (0.1:1).

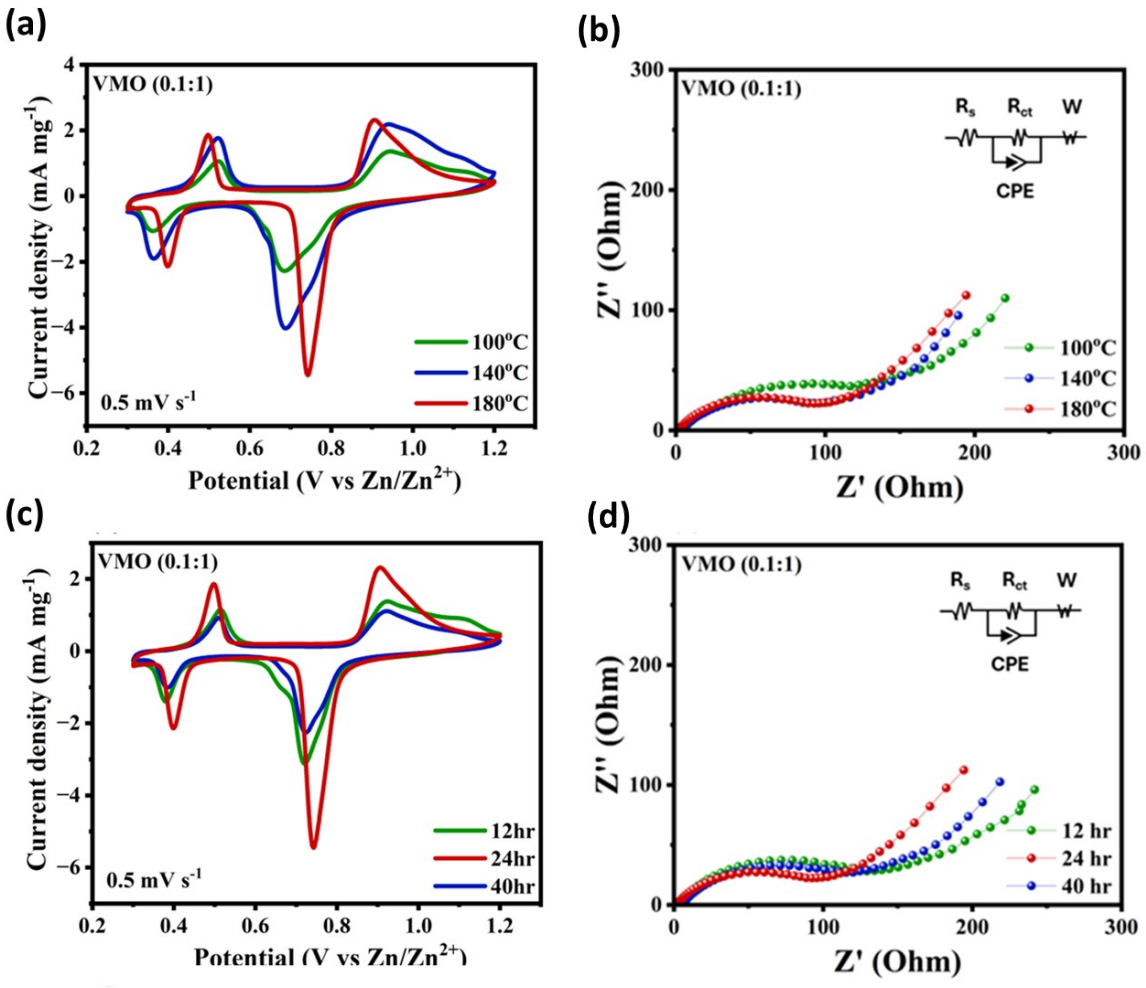

Figure S8 (a) Cyclic voltammetry curves (b) EIS of VMO (0.1:1) synthesized at different temperatures. (c) Cyclic voltammetry curves (d) EIS of VMO (0.1:1) synthesized at different times.

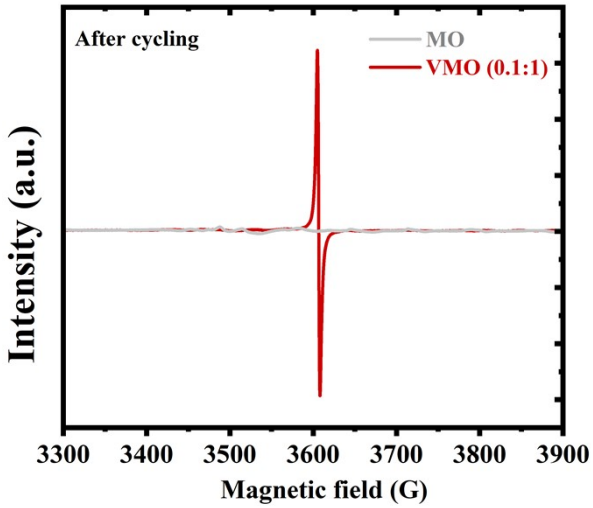

Figure S9 EPR spectra of MO and VMO (0.1:1) after 2500 cycles.

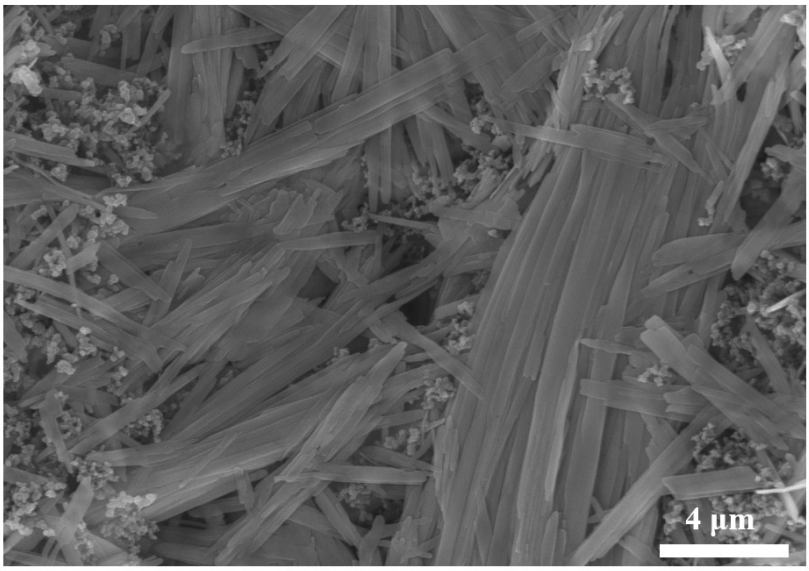

Figure S10 SEM image VMO (0.1:1) after 2500 cycles.

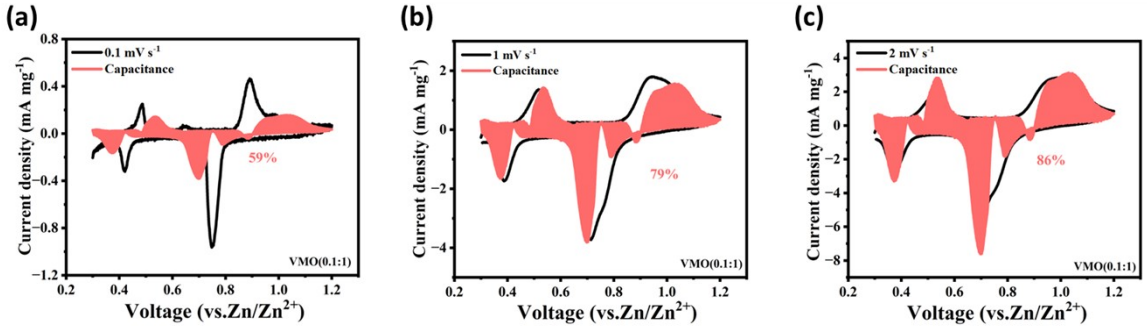

Figure S11 Cyclic voltammetry curves of VMO (0.1:1) measured at various scan rates. (a) 0.1 mV s^{-1}, (b) 1 mV s^{-1} and (c) 2 mV s^{-1}.

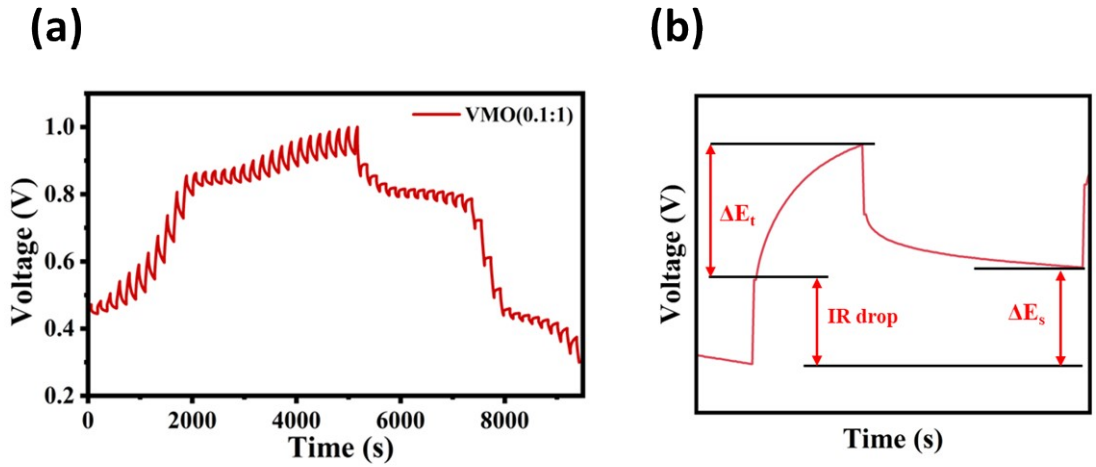

Figure S12 (a) Galvanostatic intermittent titration technique (GITT) profile of VMO (0.1:1) electrode during charge/discharge. (b) Schematic illustration of a typical GITT profile.

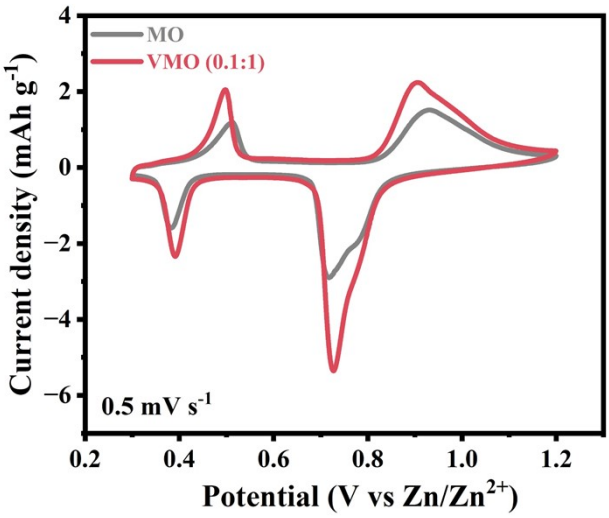

Figure S13 Cyclic voltammetry curves of MO and VMO (0.1:1) pouch cells at a scan rate of 0.5 mV s^{-1}.

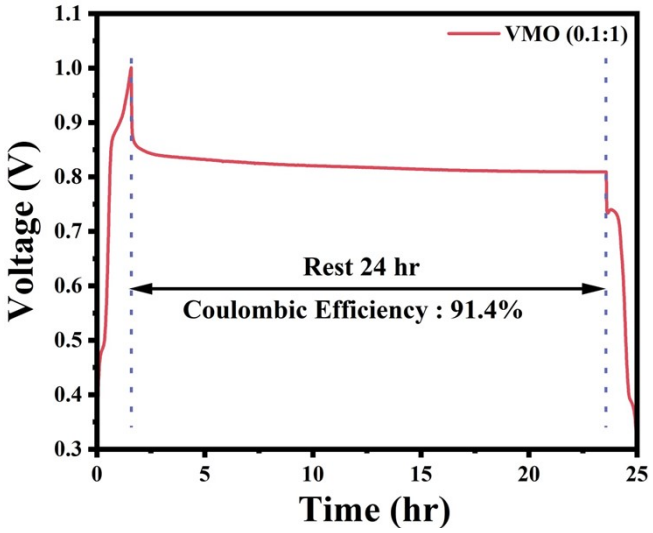

Figure S14 Voltage–time profile of the VMO (0.1:1) electrode recorded under a 24 h rest test, demonstrating stable discharge behavior after prolonged relaxation with the CE of 91.4%.

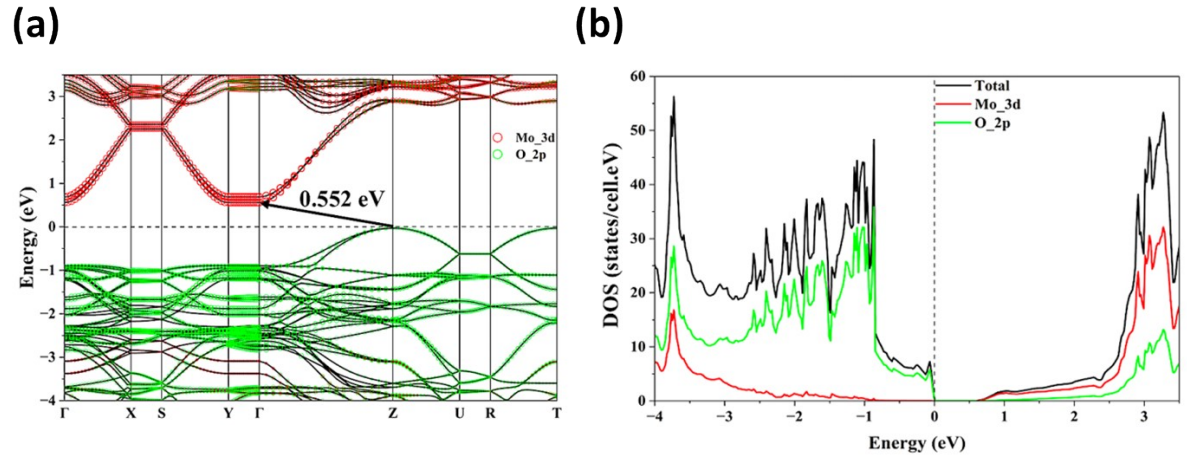

Figure S15 (a) Band structure and (b) density of states of MoO_3.

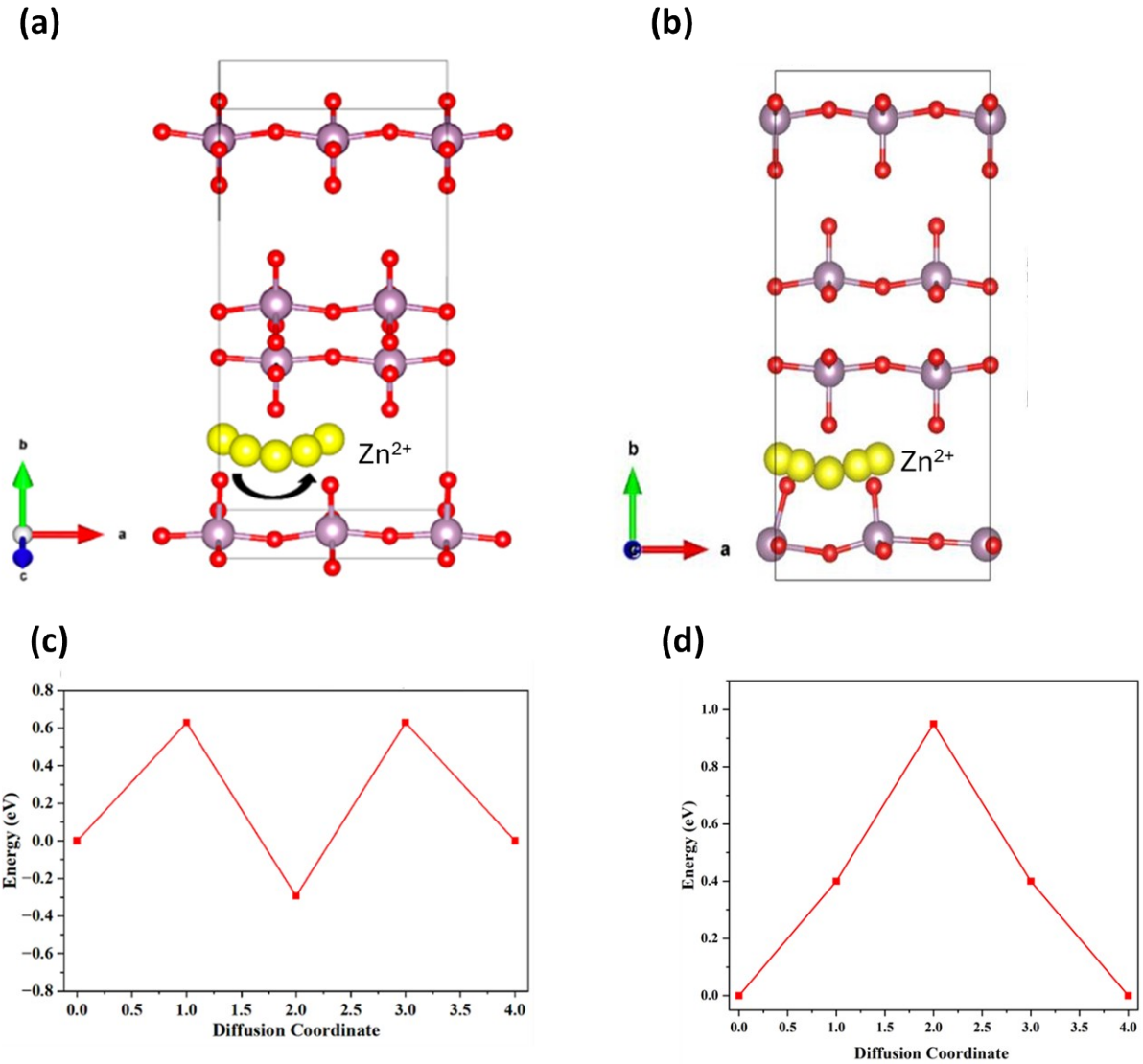

Figure S16 Diffusion pathway of Zn^{2+}(yellow) along the a-axis within (a) the ac-plane and (b) within the ab-plane and the corresponding energy barrier of Zn^{2+} along the a-axis (c) within the ac-plane and (d) within the ab-plane.

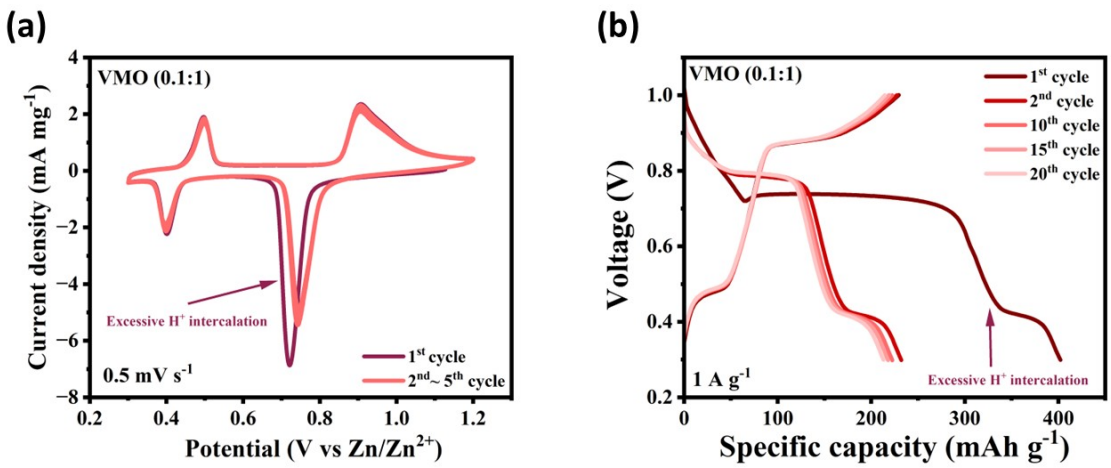

Figure S17 Electrochemical performance of VMO (0.1:1) coin cell: (a) CV curves at a scan rate of 0.5 mV s^{-1} and (b) GCD profiles at 1 A g^{-1}. The excessive H^+ intercalation during the initial cycles is highlighted.

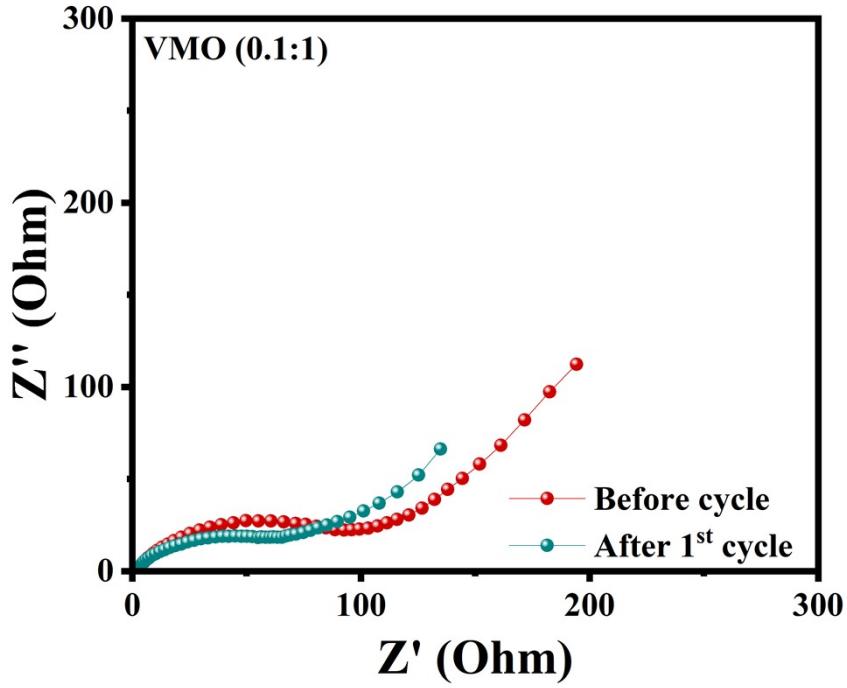

Figure S18 Electrochemical impedance spectra of VMO (0.1:1) recorded before and after the first discharge cycle.

Supplementary References

1. X. Wu, Y. Xiang, Q. Peng, X. Wu, Y. Li, F. Tang, R. Song, Z. Liu, Z. He and X. Wu, *J. Mater. Chem. A* 2017, **5**, 17990-17997.
2. G. Kresse and D. Joubert, *Phys. Rev. B*, 1999, **59**, 1758-1775.
3. W. Kohn, A. D. Becke and R. G. Parr, *J. Phys. Chem.*, 1996, **100**, 12974-12980.
4. P. E. Blöchl, *Phys. Rev. B*, 1994, **50**, 17953-17979.
5. W. Kohn and L. J. Sham, *Phys. Rev.*, 1965, **140**, A1133-A1138.
6. J. P. Perdew, K. Burke and M. Ernzerhof, *Phys. Rev. Lett.*, 1996, **77**, 3865-3868.
7. M. Wang and A. Navrotsky, *Solid State Ionics*, 2004, **166**, 167-173.
8. G. Henkelman, B. P. Uberuaga and H. Jónsson, *J. Chem. Phys.*, 2000, **113**, 9901-9904.
9. G. Henkelman and H. Jónsson, *J. Chem. Phys.* , 2000, **113**, 9978-9985.